# Magnetocaloric properties of bulk Fe2AlB2 synthesized by reactive hot isostatic pressing

Hugo R da Igreja, Sophie Tencé, Patrick Chartier, Sylvain Dubois

## To cite this version:

Hugo R da Igreja, Sophie Tencé, Patrick Chartier, Sylvain Dubois. Magnetocaloric properties of bulk Fe2AlB2 synthesized by reactive hot isostatic pressing. Journal of the European Ceramic Society, 2024, 10.1016/j.jeurceramsoc.2024.03.063 . hal-04542010

**HAL Id: hal-04542010**

**https://hal.science/hal-04542010**

Submitted on 11 Apr 2024

ARTICLE IN PRESS

Journal of the European Ceramic Society xxx (xxxx) xxx

Contents lists available at ScienceDirect

Journal of the European Ceramic Society

journal homepage: www.elsevier.com/locate/jeurceramsoc

# Magnetocaloric properties of bulk $Fe_2AlB_2$ synthesized by reactive hot isostatic pressing

Hugo R. da Igreja [a,*], Sophie Tencé [b], Patrick Chartier [a], Sylvain Dubois [a]

[a] *Institut Pprime, Université de Poitiers-CNRS-ENSMA, UPR, Poitiers 3346, France*
[b] *CNRS, Univ. Bordeaux, Bordeaux INP, ICMCB, UMR 5026, Pessac F-33600, France*

ARTICLE INFO

*Keywords:*
Fe2AlB2
MAB phases
Magnetocaloric effect
Hot isostatic pressing
Magnetic properties

ABSTRACT

This study presents a new single-step synthesis of $Fe_2AlB_2$ at 1150°C for 4 hours using hot isostatic pressing (HIPing). X-ray diffraction confirmed the material as single-phase, while metallographic etching revealed predominant equiaxial $Fe_2AlB_2$ grains (~25 μm) and minor unreacted boron particles and Al-rich zones at grain boundaries. Magnetocaloric investigations demonstrated an impressive isothermal entropy change of 2.9 J/kg.K at 2 T and 6.8 J/kg.K at 5 T, with corresponding adiabatic temperature changes of 1.1 K and 2.8 K at 2 and 5 T, respectively. The HIPed $Fe_2AlB_2$ performance matches that of studies without post-treatments or doping. $Fe_2AlB_2$, composed of light and earth-abundant elements, can be synthesized in a single step using HIPing, making it an attractive option for magnetic refrigeration with improved energy efficiency and simplified manufacturing.

## 1. Introduction

The MAB phases, nano-laminated transition-metal borides, are a class of materials that have gained significant interest in recent years because of their unique properties, suitable according to the transition metal and the stoichiometry. $Fe_2AlB_2$, an extensively researched compound, exhibits a significant magnetocaloric effect (MCE) close to room temperature (RT), making it a promising candidate for applications in magnetic refrigeration and magnetocaloric energy conversion. The crystal structure of $Fe_2AlB_2$ comprises two formula units, with Fe and B atoms forming a $Fe_2B_2$ slabs within the (ac) plane, separated by a monolayer of Al atoms aligned along the orthorhombic b-axis [1–3]. At room temperature, $Fe_2AlB_2$ shows a ferromagnetic behavior [2], however, it undergoes a ferromagnetic (FM) to paramagnetic (PM) phase transition [4,5] in the vicinity of the Curie temperature ($T_C$), which is typically reported in the range of 274–320 K [2,6–8], depending on the synthesis method employed. It is also stressed the strong coupling between the magnetic and crystallographic lattices. Additionally, it has been experimentally confirmed that the a-axis represents the easiest direction for achieving saturation magnetization, indicating the presence of anisotropic magnetic behavior in this compound [9,10].

The magnetocaloric effect can be defined as the adiabatic temperature change triggered by the application followed by the removal of an external applied magnetic field. This effect reaches the maximum when the temperature is in the proximities of the magnetic phase transition (at the Curie temperature – $T_C$) [9].

The materials driving research and development in magnetic refrigeration express a giant magnetocaloric effect near room temperature (GMCE), e.g. $Gd_5(Si_2Ge_2)$ [11], $MnFe(P_{1-x}As_x)$ [12] and Heusler alloys [13]. They can be classified as first-order magneto structural phase-transition materials (FOMTM), wherein the magnitude of the magnetic entropy change ($\Delta S_M$) is high but occurs within a limited temperature range. Other additional factors constrain the utilization of these materials on an industrial scale: the structural change during the magnetic transition, the low Curie temperature, and their abundant composition in rare earth and/or toxic elements.

On the other hand, $Fe_2AlB_2$ is a rare-earth free (RE-free) second order magnetic phase transition material (SOMTM). This transition is characterized by a gradual and continuous magnetization variation in the vicinity of $T_C$, with lower $\Delta S_M$ peaks – in comparison with FOMTM – but in a wider temperature range and weaker or non-existent magnetic and thermal hysteresis, advantageous attributes of magnetic refrigerants.

Several methods using powder metallurgy are used to synthesize $Fe_2AlB_2$ phase. Dense bulk materials, powder mixtures, and single-crystal are the final products found in the literature. Focused on bulk polycrystalline samples, some methods are often used, such as: Reactive

---

* Correspondence to: 11, Bd Pierre et Marie Curie, Institut Pprime, SP2MI, Office 1/E055, SP2MI First floor, Poitiers, Chasseneuil-du-Poitou Cedex 9 86073, France.
*E-mail address:* hugo.da.igreja@univ-poitiers.fr (H.R. da Igreja).

https://doi.org/10.1016/j.jeurceramsoc.2024.03.063
Received 9 November 2023; Received in revised form 29 February 2024; Accepted 28 March 2024

Please cite this article as: Hugo R. da Igreja et al., *Journal of the European Ceramic Society*, https://doi.org/10.1016/j.jeurceramsoc.2024.03.063

hot pressing (RHP) [14–18], spark plasma sintering (SPS) [8], vacuum suction casting [19–21], and melt spinning [9,22,23]. An alternative method for synthesizing these phases, to date not yet explored, is hot isostatic pressing (HIP). The combination of temperature and isostatic pressure can be used for upgrading castings, densifying pre-sintered components, and consolidating powders at lower temperatures and times. In terms of bulk materials, it reduces macro and micro porosity [24,25]. Therefore, the objective of this study consists of synthesizing bulk $Fe_2Al_xB_2$ (with x=1.2) by reactive HIPing process and in studying the resulting microstructure and magnetocaloric properties.

## 2. Materials and methods

### 2.1. Synthesis

Aluminum (Alfa Aesar, −100 + 325 mesh, 99.5% purity), crystalline Boron (H. C. Starck GmbH Grade P1, crystalline < 38 μm, 98/99% purity) and Iron (Alfa Aesar, −200 mesh, 99 +% purity) powders were used as starting materials. The $Fe_2AlB_2$ sample was weighted according to the molar ratio of 2Fe: 1.2Al: 2B (total mass = 4.0 g). Such an Al excess was important to balance the evaporation and to avoid FeB impurities [26]. Subsequently, the mixture was ball milled in a three-dimensional Turbula® mixer. The powder mixture was then uniaxially cold-pressed (20 MPa) in a stainless-steel mold to form a cylindrical green pellet (12 mm diameter and 6 mm height). The pellet was encapsulated into a glass container, surrounded by glass pieces, under primary vacuum ($\sim 10^{-2}$ bar) to prevent oxidation during the following heat treatment and to preserve the sample integrity. The sealed sample was heated in a hot isostatic press furnace (ACB-HIP6) to 1150°C, held at that temperature for 4 h, and pressed at 150 MPa in the last 2 h. Finally, the synthesized sample surfaces were grinded to remove glass-related impurities.

### 2.2. Characterization

Microstructural analysis was conducted using light optical (LOM – Keyence VHX700N) and scanning electron microscopy (SEM – JEOL 7710 TTLS), with the latter equipped with an energy dispersive X-ray spectroscopy (EDS – Oxford Instruments) at an accelerating voltage of 10 kV. Regarding the applied accelerating voltage and the mean sample stoichiometry, the electron-matter interaction, estimated by Monte Carlo simulations using the CASINO software [27,28], has a probed volume equivalent to a sphere of about 0.7 μm in diameter. EDS measurements were performed in specific areas and standardless quantitative analysis using the AZtec software (Oxford instrument). The relative error in concentration is estimated at ~3% for heavy elements and ~10% for light elements. Quantitative results are normalized and presented in at%.

Based on the use of a 10% NaOH aqueous solution by Alameda et al. to exfoliate the Al layer on MoAlB [29], the typical metallographic etching proposed for Al alloys [30], and Matkivskyi et al. application of NaOCl to enhance polishing in Si wafers [31], a 0.005 M NaOH + 0.01M NaOCl solution performed at 50°C was proposed as metallographic etching with the specific objective of revealing the grain boundaries of $Fe_2AlB_2$. Using ImageJ software, the grain morphology was measured in the form of equivalent diameter (or Heywood diameter) and roundness, $r = 4\,\pi\,\text{area}/(\text{perimeter})^2$.

The X-ray diffraction analysis with Bragg-Brentano geometry was performed in a Bruker D8 Advance diffractometer operating with Cu-Kα (λ= 1.5406 Å) incident radiation. The measurements were made at room temperature and the data were acquired in the 25 – 55° 2θ range with a step size of 0.007° and a time step of 4 s. The voltage and current used were 40 kV and 40 mA, respectively. The 2θ range corresponds to the one in which the peaks of the $Fe_2AlB_2$, FeB, and $Al_{13}Fe_4$ phases are of higher intensities. Rietveld refinement [32–34] was performed using FullProf software relied on the Inorganic Crystal Structure Database (ICSD). The pseudo-Voigt model was used to refine the peak shape, as well as the lattice parameters, scale factors, background parameters, atom coordinates, and preferred orientation.

### 2.3. Magnetic measurements

Magnetization as a function of temperature, M(T), and applied field, M(H), were investigated using a superconducting quantum interference device (SQUID) magnetometer (Quantum Design MPMS-7XL). The magnetization *vs* temperature M(T) measurements were performed in the 20–320 K temperature range in a constant magnetic field of 0.05 T with a temperature sweep rate of 1.5 K/min. Magnetic isotherms M(H) were recorded within the 260–320 K temperature range under applied magnetic field varying in the range of 0–5 T by steps. The ΔH steps were 0.02 T in 0–0.16 T, 0.19 T in 0.16–1.5 T and 0.5 T in 1.5–5 T. The isothermal magnetization as a function of the applied field enabled the calculation of the magnetic entropy changes $\Delta S_M(T)$ using the Maxwell relation [35–37]:

$$\Delta S_M(T) = \mu_0 \int_0^H \left(\frac{dM}{dT}\right)_H dH \qquad (1)$$

The heat capacity ($C_p$) measurements at constant pressure and zero applied field were conducted on a Quantum Design Physical Property Measurement System (PPMS) using the heat capacity option. The zero-field measurements were performed in the 2–400 K temperature range at a rate of 0.25 K/min, using the relaxation method [38]. The sample holder and Apiezon N grease signal contribution were measured and subtracted from the total result. The magnetic entropy changes were also calculated by measuring the heat capacity at constant pressure in different applied fields (0, 2 and 5 T) in the vicinity of $T_C$ (254–326 K) and using Eq. 2 [36,37]. For the non-zero field measurements the rate was increased for 0.05 K/min.

$$\Delta S_M(T) = \int_0^T \frac{Cp(T)_{H2} - Cp(T)_{H1}}{T} dT \qquad (2)$$

In both cases, the adiabatic temperature change ($\Delta T_{ad}$) was calculated through the isentropic variation between two S(H,T) curves in constant magnetic fields. To establish the S(H,T) curves, the S(H=0,T) curve, obtained from zero-field heat capacity measurements, was subtracted from the magnetic entropy change values [6].

## 3. Results and discussions

Experimental X-ray diffractogram and refined results are shown in Fig. 1. Rietveld refinement results in a single $Fe_2AlB_2$ orthorhombic structure crystallizing in the Cmmm space group with refined lattice parameters a = 2.9307(5) Å, b = 11.040(2) Å, and c = 2.8699(4) Å and

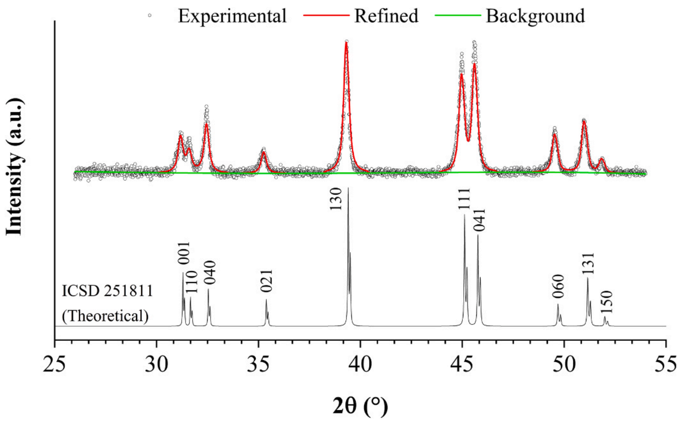

**Fig. 1.** Experimental X-ray diffractogram and corresponding refined results for the $Fe_2AlB_2$ sample. The theoretical pattern is also plotted.

the atomic positions: Fe at 4j (0, 0.3564 (1), 0.5) sites, Al at 2a (0, 0, 0) sites and B at 4i (0, 0.1988 (1), 0) sites. These values are comparable to the ones published in the literature [1,6,7,9,10,17–19,21,39].

The intensities of (0k0) reflections are higher than those of the theoretical XRD pattern referenced in ICSD 251811, revealing a slight preferential orientation (0k0) of the grains. Within the 2θ range analyzed no impurity or secondary phases are observed, however it is important to emphasize that this technique has limitations regarding the small quantity phases (~2%).

The optical micrography of the polished and etched specimen is shown in Fig. 2. Typically, studies that use chemical etching in $Fe_2AlB_2$ have traditionally focused on post-treatment processes aimed at removing impurities generated during synthesis. In contrast, this study specially targets metallographic etching to reveal grain boundaries. The stress state induced during hot isostatic pressing (HIPing) differs from other typical methods used to synthesize dense bulk $Fe_2AlB_2$, such as reactive hot pressing (RHP) and arc-melting [40]. $Fe_2AlB_2$ produced by arc-melting usually exhibit elongated plate-like [8,9] or dendritic-like [41] grains, with limited information regarding the grain shape resulting from RHP; furthermore, a different morphology is expected when using HIPing. Metallographic etching allowed a grain size estimation, indicating a mean equivalent diameter of approximately 25 µm. The observed grain shape is determined to be equiaxial, with a mean roundness of approximately 35%. A promising magnetocaloric effect is not the only requirement for magnetic refrigerator materials [42,43]. Good mechanical properties are also essential, and they are significantly influenced by the shape and size of the grains and porosity. Complementing the result obtained by XRD, it is suggested that the gray regions located in the grain boundaries and indicated by the yellow arrows on the zooming inset of Fig. 2 are impurities or secondary phases. Dark regions may represent porosity or, more likely, grain shedding during polishing.

Fig. 3 shows the scanning electron microscope (SEM) image of the polished and etched specimen in secondary electron mode (SE) to observe the general microstructure of the sample's surface. Furthermore, it highlights the grain boundaries and by the Z contrast it is possible to notice the chemical difference in some darker regions and identify the porosity.

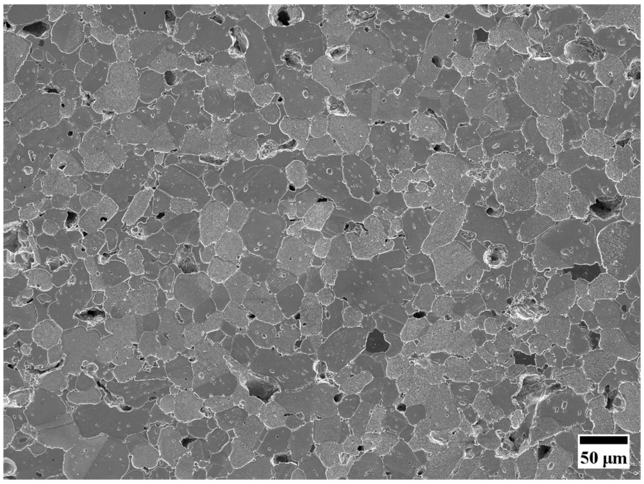

**Fig. 3.** Secondary electron SEM image of the etched $Fe_2AlB_2$ sample revealing the grains.

The SEM image of the sample, performed in backscattered electron mode (BSE) at higher magnification, and the chemical distribution, depicted by the EDS maps of Fe, Al, and B, is presented in Fig. 4. The BSE image confirms the chemical disparities at the grain boundaries and in certain dark regions of the image. Among the impurity phases commonly reported in the literature, $Al_{13}Fe_4$ and FeB are prevalent, while the presence of $Al_2O_3$ is occasionally reported [16,18,21,44]. Considering the stoichiometry, especially the Al content (molar ratio: 1.2), the formation route follows a peritectic reaction (FeB + Liq Al: $Fe_2AlB_2$) and at this concentration $Al_{13}Fe_4$ formation becomes unlikely to occur [39]. The Al EDS map corroborates the peritectic reaction where, at the grain boundaries, is noted an abundance of Al content simultaneously with a decrease in the Fe and B concentrations. On the other hand, the emergence of FeB is facilitated in cases of slow cooling, such as in arc-melting synthesis [39,41]. Examination of the Fe and B EDS maps revealed that no region exhibited a simultaneous high concentration of these elements, suggesting the absence of precipitates containing them. In particular, the B EDS map depicts a clearly defined region with an exclusive B enrichment, indicative of the presence of unreacted boron particles rather than any metal boride. Moreover, EDS quantitative analysis was performed on the yellow labeled points shown in Fig. 4. The EDS results are presented in Table 1.

The quantitative EDS analysis conducted on the darker regions (point 1 in Fig. 4) reveals a predominance of the B element (95 at%), confirming that it consists in unreacted B particles. Although BSE mode analysis alone cannot differentiate between porosity, grains pulled out during polishing, and B particles, coupling this technique with secondary electron images enables clear differentiation. Quantitative EDS analyses performed at points 2 and 7 (i.e.: on grain boundaries) indicate an average concentration of 67 at% of Al and 30.5 at% of Fe. Although the results at point 3 may suggest a stoichiometry close to that of $Al_{13}Fe_4$, the remaining examined points at the grain boundaries (2 and 4–7) do not correspond to this phase. Regarding the initial Al content (Al molar

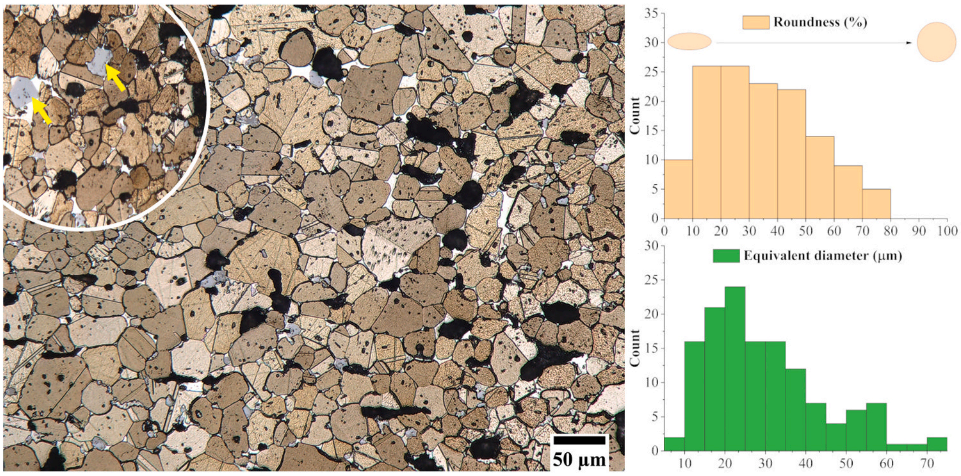

**Fig. 2.** Micrography of the $Fe_2AlB_2$ etched with the inset focusing on the unknown particles.

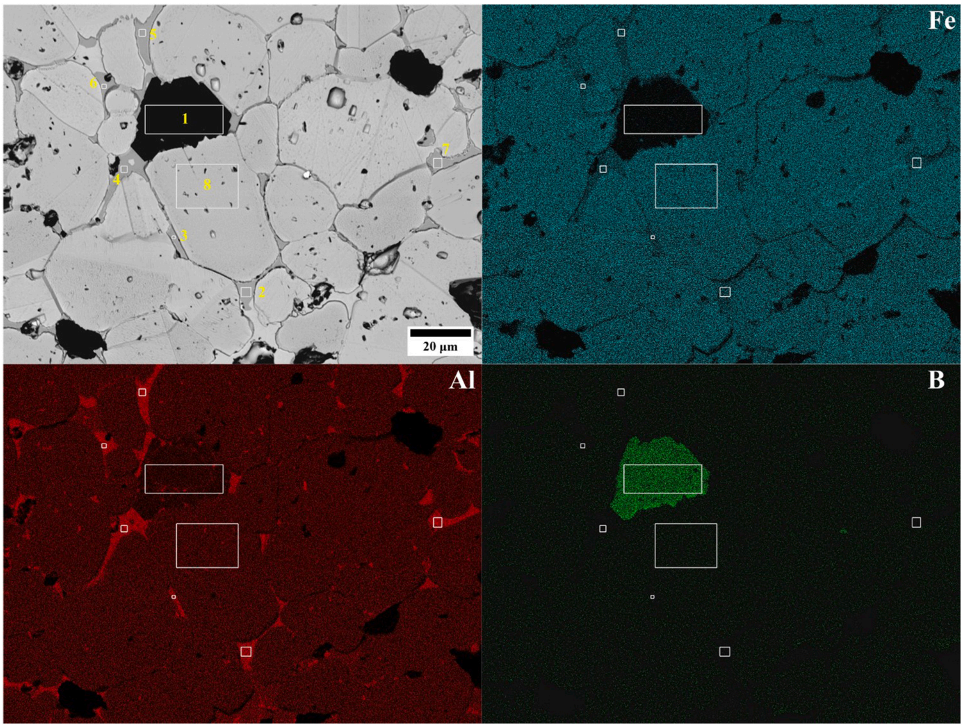

**Fig. 4.** SEM image, in backscattered electron mode (BSE), of the $Fe_2AlB_2$ sample. The yellow labelled points (1 – 8) correspond to the region in which the quantitative analysis of EDS is performed (see Table 1). EDS element distribution of Fe (cyan), Al (red) and B (green) in the $Fe_2AlB_2$ sample.

**Table 1**
Energy dispersive X-ray (EDS) quantitative measurements (at%) performed in specific points of the $Fe_2AlB_2$ sample marked in the Scanning Electron Microscopy (SEM) BSE image of Fig. 4.

| Elements Points | Fe (at%) | Al (at%) | B (at%) |
|---|---|---|---|
| 1 | 0.2 | 4.6 | 95.2 |
| 2 | 36.9 | 63.1 | 0 |
| 3 | 24.1 | 75.9 | 0 |
| 4 | 29.3 | 69.4 | 1.3 |
| 5 | 29.3 | 55.7 | 15.0 |
| 6 | 27.9 | 72.1 | 0 |
| 7 | 36.3 | 63.7 | 0 |
| 8 | 45.0 | 21.4 | 33.6 |

ratio: 1.2), XRD phase identification and refinement, and the assembly of EDS maps, it is more plausible that there exists an Al-rich zone at the grain boundaries rather than formation of a secondary phase such as $Al_{13}Fe_4$. The concentrations of elements in point 8 deviate from the ideal $Fe_2AlB_2$ stoichiometry. However, due to uncertainties in the EDS quantification method, as described in the materials and methods section, precise determination of how this material differs from ideal stoichiometry is challenging. The presence of minor unreacted boron particles has a discernible impact on grain chemical composition, though determining if this effect is localized or widespread is complex. To mitigate this issue, utilizing highly pure FeB as a starting powder in $Fe_2AlB_2$ synthesis is recommended.

The temperature dependent magnetization curve M(T), measured under a constant magnetic field of 0.05 T, is plotted in Fig. 5. A spontaneous magnetization is observed, indicating ferromagnetic phase transition. The inset of the figure shows the derivative of the magnetization with respect to temperature. It allows the determination of the Curie temperature, which is about 295.5 K.

The inset in Fig. 6 shows the heat capacity ($C_p$) measurements of $Fe_2AlB_2$ at a constant pressure as a function of temperature in zero magnetic field with results comparable with the literature [20,45]. The peak, in the proximity of 295 K, agrees with the M(T) curve and is related to the ferromagnetic to paramagnetic (FM-PM) phase transition. The heat capacity measured in 0, 2 and 5 T magnetic fields, with a higher measurement rate (0.05 K/min), is also plotted around the transition temperature.

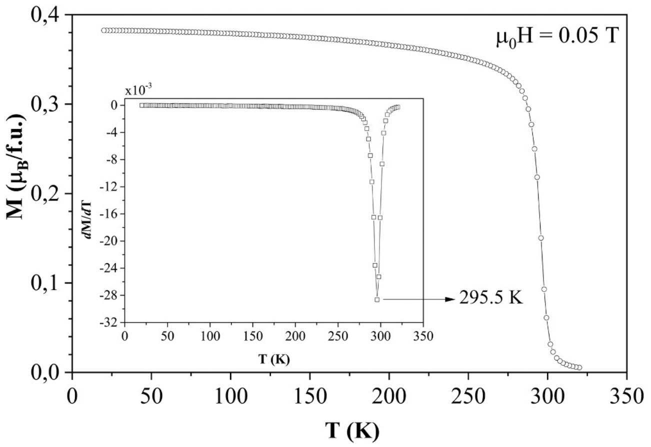

**Fig. 5.** Magnetization measured as a function of temperature – M(T) – in an applied field of 0.05 T. The inset shows the derivative of the magnetization with respect to temperature, indicating the transition temperature.

Fig. 7 shows the field dependent magnetization M(H) data measured at different temperatures in an applied magnetic field in the range 0 – 5 T. Below $T_C$ (around 295 K), the curves exhibit a ferromagnetic behavior and almost reach saturation at 5 T. The magnetic moment is 1.65 $\mu_B$/f.u. at 5 T in 260 K isotherm and is included in the range usually found in the literature [2,6,10,18,21–23,46]. As expected, an inflection of the magnetization curve is observed in the 280 – 308 K temperature range.

Fig. 8 shows the variation of the magnetic entropy change as a function of the temperature – $-\Delta S_M(T)$ – for the $Fe_2AlB_2$ sample assessed

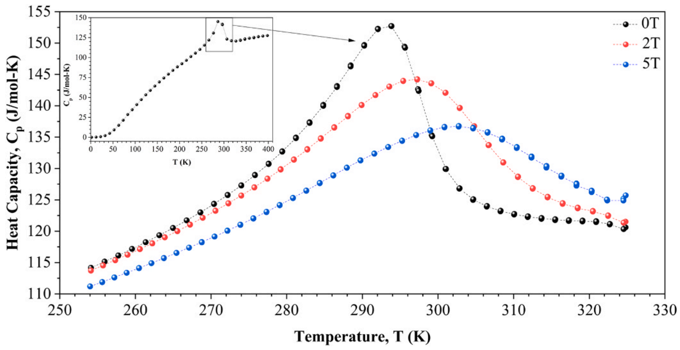

**Fig. 6.** Molar heat capacity of $Fe_2AlB_2$ sample in 0, 2 and 5 T magnetic fields as a function of temperature – $C_p(T)$ – in the vicinity of the magnetic transition. The inset shows the whole curve measured at zero magnetic field.

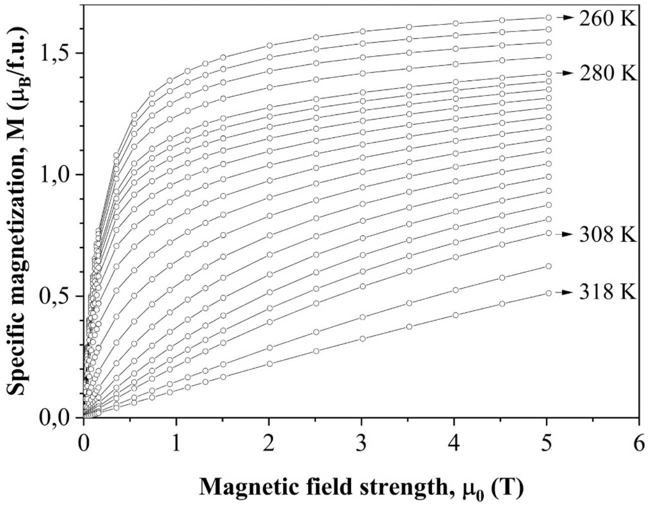

**Fig. 7.** Isothermal magnetization curves – M(H) – measured at different temperatures and in applied field in the range 0 – 5 T. The temperature step used was $\Delta T$= 5 K, 2 K and 5 K in the range of 260 – 280 K, 280 – 308 K and 308 – 318 K, respectively.

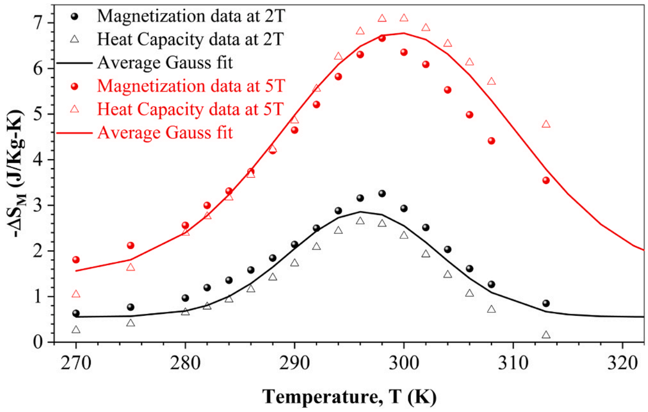

**Fig. 8.** Magnetic entropy changes *vs* temperature – $-\Delta S_M$ (T) – for the $Fe_2AlB_2$ sample calculated from heat capacity and isothermal magnetization measurements. The red and black lines are fitted results obtained using the Gauss function.

using both the heat capacity measurement technique and the isothermal magnetization one. Additionally, the fitted curve is obtained by applying the Gauss function to the average results of the methods.

The maximum entropy change, in the vicinity of $T_C$, determined from the Gauss fit, are $-\Delta S_M$ = 2.9 and 6.8 J/kg.K for applied field change $\Delta H$= 2 and 5 T, respectively. Fig. 9 compare the $-\Delta S_M$ data found in other $Fe_2AlB_2$ references with the one calculated in this investigation at $\Delta H$= 2 T. The results of the references were clustered according to post-treatment as well as the use of doping elements.

Compared to $Fe_2AlB_2$ single crystals synthesized by acid treatment (points a and b), the results of $Fe_2AlB_2$ produced by HIPing were approximatively 20% lower. It is worth mentioning that acid treatments typically use corrosive HCl as an etching agent. In relation to studies that only used annealing treatment (points c – f), our result is comparable. However, the lengthy annealing time of 72 h, as reported in the referenced works, poses a disadvantage for large-scale industrial production. The study reporting the result at point c [45] was conducted in single crystals. Additionally, simple doping focusing on Fe elemental substitution, such as Co [8] (point g) and Mn [23] (point h), did not yield significant improvements in the magnetocaloric properties of $Fe_2AlB_2$. Indeed, the results were slightly lower than those obtained in our study. Conversely, syntheses that combined post-treatments, in order to eliminate impurities, with annealing (PT and A; points i – k) and doping with annealing (D and A; points l and m) exhibit superior performance. The PT and A results outperformed HIPed $Fe_2AlB_2$ by 25%, while D and A presented an even greater improvement of 42%. Notably, point l, which represents doping (Ga and Ge [19]) with expensive and scarce elements, significantly contributed to the substantial difference between the averages.

In a comprehensive analysis, the $Fe_2AlB_2$ HIPed sample yielded slightly lower result (~15%) than the global average indicated by the red line. However, compared to literature values without additional treatments or doping, our findings fall within the average range. This fact strengthens the effectiveness of the HIP method for straightforward single-step synthesis of $Fe_2AlB_2$ in its final form without the use of rare or costly elements, hazardous acid treatments, and prolonged annealing treatments as a cost-effective processing technique.

Another important performance parameter is the refrigeration cooling power (RCP), expressed in Eq. 3. This figure of merit measures the “energy taken” capabilities of the material through the peak value ($-\Delta S_M$) and the full width at half maximum (FWHM) of the magnetic entropy change *vs* temperature curve.

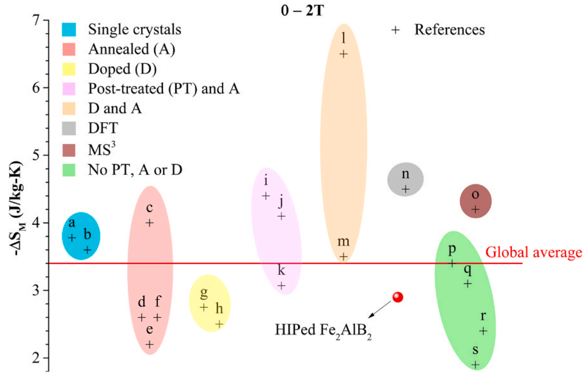

**Fig. 9.** Magnetic entropy change found in this study (red dot) and in the literature for an applied field variation of $\Delta H$ = 2 T, grouped under their specific synthesis conditions. a. [10] Al flux growth; b. [9] Arc-melting; c. [45] Arc-melting / Bridgeman Technique; d. [20] Suction cast; e. [20] LENS™ printed rod sample; f. [21] Drop-casting and annealing; g. [8] Spark plasma sintering of $AlFe_{2-x}Co_xB_2$; h. [23]Melt spinning of $AlFe_{2-x}Mn_xB_2$; i. [6] Arc-melting Al flux; j. [6] Arc-melting Ga flux; k. [3,44] Arc-melted; l. [19] Suction- casted $Al_{1.1}Ge_{0.05}Ga_{0.05}Fe_2B_2$; m. [21] Drop-casted and annealed $Al_{1.05}Si_{0.15}Fe_2B_2$; n. [47] DFT; o. [48] Molten salt sintered/sintering (MS$^3$); p. [22,23] Melt spinning; q. [8] Spark plasma Sintering; r. [18] Reactive Hot press; s. [3] Arc-melting.

$$RCP = FWHM. \left[ -\Delta S_M \quad \right]_{T=T_C} \tag{3}$$

The RCP calculated from the fitted curves are 39 J/ kg and 142 J/ kg at 2 T and 5 T, respectively. The values obtained through the Gauss fit function are lower than those reported in the existing literature [6, 21–23,44]. It is pertinent to point that there is a scarcity of studies presenting calculated RCP values for this phase, and the instances where such values are provided, the methodology employed typically does not involve curve fitting.

Fig. 10 shows the adiabatic temperature change as a function of temperature – $\Delta T_{ad}(T)$. It is calculated from the fit by a Gauss function of the average $T_{ad.}$ determined from the two methods (isothermal magnetization curves and heat capacity). At 2 T the maximum adiabatic temperature change is 1.1 K while it is 2.8 K at 5 T.

Regarding the suitability of magnetocaloric materials for use in magnetic refrigeration and magnetocaloric energy conversion, several parameters must be considered. While the magnetic entropy change ($\Delta S_M$) and adiabatic temperature change ($\Delta T_{ad}$) are commonly scrutinized in the literature, the refrigeration cooling power (RCP) emerges as a pertinent parameter for evaluating magnetocaloric properties. A potentially favored material for magnetocaloric applications should present both a large magnetic entropy changes and temperature span. Equally significant is the proximity of the transition temperature ($T_C$) to room temperature, a vital aspect for industrial utilization. Operational considerations demand the absence of both thermal and magnetic hysteresis, as well as the preservation of the material’s structural integrity throughout its use. Considering the materials used: cost, availability and toxicity are constraints. These factors collectively determine the effectiveness and applicability of magnetocaloric materials in the field of magnetic refrigeration and energy conversion.

To place the findings in a broader context, the $Fe_2AlB_2$ HIPed sample has yielded $\Delta S_M$ (magnetic entropy change) values around room temperature (295.5 K) which are notably lower than well-known giant magnetocaloric effect (GMCE) materials with $T_C$ at the same range such as $Gd_5Si_2Ge_2$ (276 K) [11], MnFe(P, Si, B) systems (230–318 K) [49–51], and $LaFeSi_{13}$ and hybrids (203–288 K) [52,53]. However, the formers GMCE materials cited presents a FOMT, with a high value of magnetic entropy change but in a narrow span of temperature and considerable thermal and magnetic hysteresis. Therefore, the SOMT compounds offer an advantage in terms of the temperature window of the phenomenon and structure stability.

Deepening the analysis, it is pertinent to compare $Fe_2AlB_2$ HIPed with materials undergoing the same type of transition. Concerning SOMT materials with magnetic phase transitions closer to room temperature (RT), $Fe_2AlB_2$ exhibits comparable values. Gadolinium (Gd), often considered as a reference for SOMT materials with $T_C$ near RT in magnetic refrigeration applications, presented 5.2 J/kg.K at 292 K under 2 T field. Gd-based alloys as $Gd_6M_{5/3}Si_3$ (M= Co and Ni) and GdY presented 2.9 – 5 J/kg.K at 278–310 K under 2 T field [54,55]. La-systems as: $La_{(1-x)}A_xMnO_3$ (A= K, Ca, and Ba) presented 1.8–3.6 J/kg.K at 213–334 K under 1 T field [54,56] and $La_{(1-x)}Sr_xCoO_3$ presented 2.5–2.7 J/kg.K at 182–253 K under 5 T field regarding the Sr content [57].

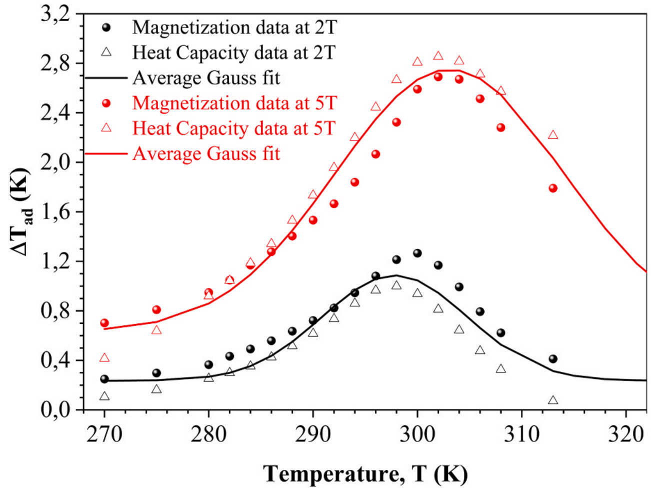

**Fig. 10.** Adiabatic temperature change as a function of temperature – $\Delta T_{ad}(T)$ – determined from the two methods (isothermal magnetization and heat capacity measurements). Red and black lines are fit with Gauss function.

Hence, it is reinforced that $Fe_2AlB_2$ emerges as a promising candidate for magnetic refrigeration applications on a large scale. Its composition of rare-earth-free and abundant elements represents an inherent advantage and reduces the material criticality [54] concerning the cost, availability, and environmental impact. Notably, HIPed $Fe_2AlB_2$ exhibits MCE performance comparable to further treated counterparts, yet benefits from a single-step synthesis method, optimizing production without the need for extra manufacturing processes.

The Al content in $Fe_2AlB_2$ significantly impacts its microstructure and phase composition. As the Al content increases, the presence of the FeB phase decreases gradually, while a too large Al excess lead to the formation of the $Al_{13}Fe_4$ phase. Additionally, the Al content dictates how $Fe_2AlB_2$ forms, either through a peritectic reaction (Al<1.4) or through direct nucleation (Al>1.4) and it influences $Fe_2AlB_2$ cell parameters [39]. The magnetic properties are closely tied to the distance between the magnetic atoms, particularly Fe-Fe and Fe-B atoms in the $Fe_2B_2$ chains within the (ac)-plane [19]. A higher Al composition tends to reduce cell parameters, impacting magnetoelastic coupling. Han et al. [39] work shows that $Fe_2AlB_2$ formed through a peritectic reaction exhibits superior MCE performance compared to $Fe_2AlB_2$ formed by direct crystallization. They propose that MCE performance can be enhanced further by controlling solidification behaviors and annealing to increase the unit cell volume and improve magnetoelastic coupling. Our investigation indicates that HIPed $Fe_2AlB_2$ follows the peritectic route formation, therefore future studies should explore the effects of post-homogenization annealing to enhance the magnetocaloric properties of HIP-processed $Fe_2AlB_2$.

## 4. Conclusions

The microstructure, grain morphology, magnetic and magnetocaloric properties of $Fe_2AlB_2$ synthesized by hot isostatic pressing (HIP) method were fully investigated. The sample, metallographically etched with a 0.005 M NaOH + 0.01 M NaOCl solution with the sole purpose of revealing the grain boundaries, enables the study of the grain’s morphology. The light optical microscopy (LOM) shows an equiaxial grain with, in average, 25 µm size. Still in the LOM analysis, it was possible to visualize the presence of impurities in the grain boundaries. This analysis extended to SEM and EDS investigations showed Al segregation at the grain boundary, consequence of the peritectic reaction, besides the minor presence of unreacted boron particles. The magnetic M(T) measurements showed that the sample undergoes a second order ferromagnetic phase transition in the vicinity of 295.5 K. For an applied field changes of 2 T and 5 T, the peak of the magnetic entropy change is 2.9 J/kg.K and 6.8 J/kg.K, respectively. Adiabatic temperature change values are 1.1 K and 2.8 K at 2 T and 5 T, respectively. The refrigeration cooling powers are 39 J/kg and 142 J/kg for the same applied fields changes. Comparatively, the $Fe_2AlB_2$ HIPed sample exhibited slightly lower results (~15%) than other syntheses reported in the literature. However, regarding studies without post-treatments or doping, the outcomes are comparable. Therefore, it confers a significant advantage to HIPing method in terms of employing a single-step approach without further manufacturing process. It is imperative to point out that the resulting $Fe_2AlB_2$ still contains few unreacted boron particles that may decrease its performance and can be avoided by using high-purity FeB as the initial powder instead of separate Fe and B powders. Noteworthy that no additional post-treatments were undertaken, and no doping elements were introduced to improve the magnetocaloric characteristics. Therefore, by the promising features of the material and the simplicity of the synthesis method, the Fe$_2$AlB$_2$ obtained by HIPing process is an attractive alternative from an industrial point of view.

## CRediT authorship contribution statement

DA IGREJA, Hugo: Conceptualization, Investigation, Formal analysis, Visualization, Writing - Original Draft. TENCÉ, Sophie: Investigation, Writing - Review & Editing. CHARTIER, Patrick: Supervision, Writing - Review & Editing. DUBOIS, Sylvain: Supervision, Project administration, Funding acquisition, Conceptualization, Writing - Review & Editing

## Declaration of Competing Interest

The authors declare that they have no known competing financial interests or personal relationships that could have appeared to influence the work reported in this paper.

## Acknowledgements

The authors thank the Ministère de l'Enseignement Supérieur et de la Recherche and the French government program “Investissements d'Avenir” (EUR INTREE, reference ANR-18-EURE-0010). This work pertains to the France 2030 program “Investissements d'Avenir” (LABEX INTERACTIFS, reference ANR-11-LABEX-0017–01).

## References

[1] W. Jeitschko, The crystal structure of Fe2AlB2, Acta Cryst. B 25 (1969) 163–165, https://doi.org/10.1107/S0567740869001944.

[2] M. ElMassalami, D. da, S. Oliveira, H. Takeya, On the ferromagnetism of AlFe2B2, J. Magn. Magn. Mater. 323 (2011) 2133–2136, https://doi.org/10.1016/j.jmmm.2011.03.008.

[3] J.W. Lee, M.S. Song, K.K. Cho, B.K. Cho, C. Nam, Magnetocaloric properties of AlFe2B2 including paramagnetic impurities of Al13Fe4, J. Korean Phys. Soc. 73 (2018) 1555–1560, https://doi.org/10.3938/jkps.73.1555.

[4] L.H. Lewis, R. Barua, B. Lejeune, Developing magnetofunctionality: coupled structural and magnetic phase transition in AlFe2B2, J. Alloy. Compd. 650 (2015) 482–488, https://doi.org/10.1016/j.jallcom.2015.07.255.

[5] T. Ali, M.N. Khan, E. Ahmed, A. Ali, Phase analysis of AlFe2B2 by synchrotron X-ray diffraction, magnetic and Mössbauer studies, Prog. Nat. Sci.: Mater. Int. 27 (2017) 251–256, https://doi.org/10.1016/j.pnsc.2017.03.007.

[6] X. Tan, P. Chai, C.M. Thompson, M. Shatruk, Magnetocaloric Effect in AlFe2B2: toward magnetic refrigerants from earth-abundant elements, J. Am. Chem. Soc. 135 (2013) 9553–9557, https://doi.org/10.1021/ja404107p.

[7] J. Cedervall, M.S. Andersson, T. Sarkar, E.K. Delczeg-Czirjak, L. Bergqvist, T. C. Hansen, P. Beran, P. Nordblad, M. Sahlberg, Magnetic structure of the magnetocaloric compound AlFe2B2, J. Alloy. Compd. 664 (2016) 784–791, https://doi.org/10.1016/j.jallcom.2015.12.111.

[8] S. Hirt, F. Yuan, Y. Mozharivskyj, H. Hillebrecht, AlFe2–xCoxB2 (x = 0–0.30): TC tuning through co substitution for a promising magnetocaloric material realized by spark plasma sintering, Inorg. Chem. 55 (2016) 9677–9684, https://doi.org/10.1021/acs.inorgchem.6b01467.

[9] R. Barua, B.T. Lejeune, L. Ke, G. Hadjipanayis, E.M. Levin, R.W. McCallum, M. J. Kramer, L.H. Lewis, Anisotropic magnetocaloric response in AlFe2B2, J. Alloy. Compd. 745 (2018) 505–512, https://doi.org/10.1016/j.jallcom.2018.02.205.

[10] T.N. Lamichhane, L. Xiang, Q. Lin, T. Pandey, D.S. Parker, T.-H. Kim, L. Zhou, M. J. Kramer, S.L. Bud'ko, P.C. Canfield, Magnetic properties of single crystalline itinerant ferromagnet ${\mathrm{AlFe}}_{2}{\mathrm{B}}_{2}$, Phys. Rev. Mater. 2 (2018) 084408 https://doi.org/10.1103/PhysRevMaterials.2.084408.

[11] V.K. Pecharsky, K.A. Gschneidner Jr., Giant Magnetocaloric effect in ${\mathrm{Gd}}_{5}({\mathrm{Si}}_{2}{\mathrm{Ge}}_{2})$, Phys. Rev. Lett. 78 (1997) 4494–4497, https://doi.org/10.1103/PhysRevLett.78.4494.

[12] O. Tegus, E. Brück, K.H.J. Buschow, F.R. de Boer, Transition-metal-based magnetic refrigerants for room-temperature applications, Nature 415 (2002) 150–152, https://doi.org/10.1038/415150a.

[13] V.K. Sharma, M.K. Chattopadhyay, R. Kumar, T. Ganguli, P. Tiwari, S.B. Roy, Magnetocaloric effect in Heusler alloys Ni50Mn34In16 and Ni50Mn34Sn16, J. Phys.: Condens. Matter 19 (2007) 496207, https://doi.org/10.1088/0953-8984/19/49/496207.

[14] N. Li, Y. Bai, S. Wang, Y. Zheng, F. Kong, X. Qi, R. Wang, X. He, A.I. Duff, Rapid synthesis, electrical, and mechanical properties of polycrystalline Fe2AlB2 bulk from elemental powders, J. Am. Ceram. Soc. 100 (2017) 4407–4411, https://doi.org/10.1111/jace.15058.

[15] J. Liu, S. Li, B. Yao, J. Zhang, X. Lu, Y. Zhou, Thermal stability and thermal shock resistance of Fe2AlB2, Ceram. Int. 44 (2018) 16035–16039, https://doi.org/10.1016/j.ceramint.2018.06.042.

[16] J. Liu, S. Li, B. Yao, S. Hu, J. Zhang, W. Yu, Y. Zhou, Rapid synthesis and characterization of a nanolaminated Fe2AlB2 compound, J. Alloy. Compd. 766 (2018) 488–497, https://doi.org/10.1016/j.jallcom.2018.06.352.

[17] Y. Bai, D. Sun, N. Li, F. Kong, X. Qi, X. He, R. Wang, Y. Zheng, High-temperature mechanical properties and thermal shock behavior of ternary-layered MAB phases Fe2AlB2, Int. J. Refract. Met. Hard Mater. 80 (2019) 151–160, https://doi.org/10.1016/j.ijrmhm.2019.01.010.

[18] S.P. Bennett, S. Kota, H. ElBidweihy, J.F. Parker, L.A. Hanner, P. Finkel, M. W. Barsoum, Magnetic and magnetocaloric properties of Fe2AlB2 synthesized by single-step reactive hot pressing, Scr. Mater. 188 (2020) 244–248, https://doi.org/10.1016/j.scriptamat.2020.07.042.

[19] R. Barua, B.T. Lejeune, B.A. Jensen, L. Ke, R.W. McCallum, M.J. Kramer, L. H. Lewis, Enhanced room-temperature magnetocaloric effect and tunable magnetic response in Ga-and Ge-substituted AlFe2B2, J. Alloy. Compd. 777 (2019) 1030–1038, https://doi.org/10.1016/j.jallcom.2018.10.206.

[20] B.T. Lejeune, R. Barua, E. Simsek, R.W. McCallum, R.T. Ott, M.J. Kramer, L. H. Lewis, Towards additive manufacturing of magnetocaloric working materials, Materialia 16 (2021) 101071, https://doi.org/10.1016/j.mtla.2021.101071.

[21] M. Sakhawat Hossain, K. Stillwell, S. Agbo, A.K. Pathak, M. Khan, The effect of Si doping on the magnetic and magneto-thermal properties of Al rich Al1.2-xSixFe2B2 intermetallic system, J. Magn. Magn. Mater. 571 (2023) 170576, https://doi.org/10.1016/j.jmmm.2023.170576.

[22] Q. Du, G. Chen, W. Yang, Z. Song, M. Hua, H. Du, C. Wang, S. Liu, J. Han, Y. Zhang, J. Yang, Magnetic properties of AlFe2B2 and CeMn2Si2 synthesized by melt spinning of stoichiometric compositions, Jpn. J. Appl. Phys. 54 (2015) 053003, https://doi.org/10.7567/JJAP.54.053003.

[23] Q. Du, G. Chen, W. Yang, J. Wei, M. Hua, H. Du, C. Wang, S. Liu, J. Han, Y. Zhang, J. Yang, Magnetic frustration and magnetocaloric effect in AlFe2−xMnxB2 (x = 0–0.5) ribbons, J. Phys. D: Appl. Phys. 48 (2015) 335001, https://doi.org/10.1088/0022-3727/48/33/335001.

[24] M.H. Bocanegra-Bernal, Hot Isostatic Pressing (HIP) technology and its applications to metals and ceramics, J. Mater. Sci. 39 (2004) 6399–6420, https://doi.org/10.1023/B:JMSC.0000044878.11441.90.

[25] H.V. Atkinson, S. Davies, Fundamental aspects of hot isostatic pressing: an overview, Met. Mat. Trans. A 31 (2000) 2981–3000, https://doi.org/10.1007/s11661-000-0078-2.

[26] S. Kota, M. Sokol, M.W. Barsoum, A progress report on the MAB phases: atomically laminated, ternary transition metal borides, Int. Mater. Rev. 65 (2020) 226–255, https://doi.org/10.1080/09506608.2019.1637090.

[27] P. Hovington, D. Drouin, R. Gauvin, CASINO: A new monte carlo code in C language for electron beam interaction —part I: description of the program, Scanning 19 (1997) 1–14, https://doi.org/10.1002/sca.4950190101.

[28] D. Drouin, A.R. Couture, D. Joly, X. Tastet, V. Aimez, R. Gauvin, CASINO V2.42—A fast and easy-to-use modeling tool for scanning electron microscopy and microanalysis users, Scanning 29 (2007) 92–101, https://doi.org/10.1002/sca.20000.

[29] L.T. Alameda, P. Moradifar, Z.P. Metzger, N. Alem, R.E. Schaak, TopochemicaL Deintercalation of Al from MoAlB: stepwise etching pathway, layered intergrowth structures, and two-dimensional MBene, J. Am. Chem. Soc. 140 (2018) 8833–8840, https://doi.org/10.1021/jacs.8b04705.

[30] M. Warmuzek, Metallographic Techniques for Aluminum and Its Alloys, (2004). https://doi.org/10.31399/asm.hb.v09.a0003769.

[31] V. Matkivskyi, A. Karstein Røyset, G. Stokkan, P. Tetlie, M. Di Sabatino, G. Tranell, Novel technique to study the wet chemical etching response of multi-crystalline silicon wafers, Mater. Sci. Eng.: B 290 (2023) 116343, https://doi.org/10.1016/j.mseb.2023.116343.

[32] D.L. Bish, S.A. Howard, Quantitative phase analysis using the Rietveld method, J. Appl. Cryst. 21 (1988) 86–91, https://doi.org/10.1107/S0021889887009415.

[33] L.B. McCusker, R.B. Von Dreele, D.E. Cox, D. Louër, P. Scardi, Rietveld refinement guidelines, J. Appl. Cryst. 32 (1999) 36–50, https://doi.org/10.1107/S0021889898009856.

[34] I.C. Madsen, N.V.Y. Scarlett, D.P. Riley, M.D. Raven, Quantitative Phase Analysis Using the Rietveld Method. Modern Diffraction Methods, John Wiley & Sons, Ltd, 2012, pp. 283–320, https://doi.org/10.1002/9783527649884.ch10.

[35] T. Hashimoto, T. Numasawa, M. Shino, T. Okada, Magnetic refrigeration in the temperature range from 10 K to room temperature: the ferromagnetic refrigerants, Cryogenics 21 (1981) 647–653, https://doi.org/10.1016/0011-2275(81)90254-X.

[36] V.K. Pecharsky, K.A. Gschneidner Jr., Magnetocaloric effect from indirect measurements: magnetization and heat capacity, J. Appl. Phys. 86 (1999) 565–575, https://doi.org/10.1063/1.370767.

[37] V.K. Pecharsky, K.A. Gschneidner, A.O. Pecharsky, A.M. Tishin, Thermodynamics of the magnetocaloric effect, Phys. Rev. B 64 (2001) 144406, https://doi.org/10.1103/PhysRevB.64.144406.

[38] P.F. Rosen, B.F. Woodfield, Standard methods for heat capacity measurements on a quantum design physical property measurement system, J. Chem. Thermodyn. 141 (2020) 105974, https://doi.org/10.1016/j.jct.2019.105974.

[39] Kun Han, Ming Li, Meng Gao, Xinming Wang, Juntao Huo, Jun-Qiang Wang, Improved magnetocaloric effects in AlFe2B2 intermetallics through the enhancement of magnetoelastic coupling, 164663–164663, J. Alloy. Compd. (2022), https://doi.org/10.1016/j.jallcom.2022.164663.

[40] R.M. German, Chapter Ten - Sintering With External Pressure, in: R.M. German (Ed.), Sintering: From Empirical Observations to Scientific Principles, Butterworth-

Heinemann, Boston, 2014, pp. 305–354, https://doi.org/10.1016/B978-0-12-401682-8.00010-0.

[41] E.M. Levin, B.A. Jensen, R. Barua, B. Lejeune, A. Howard, R.W. McCallum, M. J. Kramer, L.H. Lewis, Effects of Al content and annealing on the phases formation, lattice parameters, and magnetization of $\mathrm{A}{\mathrm{l}}_{x}\mathrm{F}{\mathrm{e}}_{2}{\mathrm{B}}_{2}\phantom{\rule{4pt}{0ex}}(x=1.0,1.1,1.2)$ alloys, Phys. Rev. Mater. 2 (2018) 034403, https://doi.org/10.1103/PhysRevMaterials.2.034403.

[42] H. Zhang, Y. Sun, E. Niu, F. Hu, J. Sun, B. Shen, Enhanced mechanical properties and large magnetocaloric effects in bonded La(Fe, Si)13-based magnetic refrigeration materials, Appl. Phys. Lett. 104 (2014) 062407, https://doi.org/10.1063/1.4865236.

[43] X.C. Zhong, D.R. Peng, X.T. Dong, J.H. Huang, H. Zhang, Y.L. Huang, S.M. Wu, H. Y. Yu, W.Q. Qiu, Z.W. Liu, R.V. Ramanujan, Improvement in mechanical and magnetocaloric properties of hot-pressed La(Fe,Si)13/La70Co30 composites by grain boundary engineering, Mater. Sci. Eng.: B 263 (2021) 114900, https://doi.org/10.1016/j.mseb.2020.114900.

[44] J.W. Lee, M.S. Song, B.K. Cho, C. Nam, Magnetic properties of pure AlFe2B2 formed through annealing followed by acid-treatment, Curr. Appl. Phys. 19 (2019) 933–937, https://doi.org/10.1016/j.cap.2019.05.004.

[45] B.T. Lejeune, D.L. Schlagel, B.A. Jensen, T.A. Lograsso, M.J. Kramer, L.H. Lewis, Effects of Al and Fe solubility on the magnetofunctional properties of ${\mathrm{AlFe}}_{2}{\mathrm{B}}_{2}$, Phys. Rev. Mater. 3 (2019) 094411 https://doi.org/10.1103/PhysRevMaterials.3.094411.

[46] Y. Bai, X. Qi, X. He, G. Song, Y. Zheng, B. Hao, H. Yin, J. Gao, A. Ian Duff, Experimental and DFT insights into elastic, magnetic, electrical, and thermodynamic properties of MAB-phase Fe2AlB2, J. Am. Ceram. Soc. 103 (2020) 5837–5851, https://doi.org/10.1111/jace.17205.

[47] A. Loudaini, M. Aggour, L. Bahmad, O. Mounkachi, Magnetic properties, magnetocaloric effect and cooling performance of AlFe2B2 compound: Ab initio, Monte Carlo and numerical modeling study, Mater. Sci. Eng.: B 264 (2021) 114935, https://doi.org/10.1016/j.mseb.2020.114935.

[48] V. Sharma, M. Dey, A. Duong, S. Gupta, R. Barua, Magnetofunctional response of AlFe2B2 powders synthesized in open air via molten salt shielded/sintering method, MRS Commun. 13 (2023) 574–580, https://doi.org/10.1557/s43579-023-00385-8.

[49] H. Wada, Y. Tanabe, Giant magnetocaloric effect of MnAs1−xSbx, Appl. Phys. Lett. 79 (2001) 3302–3304, https://doi.org/10.1063/1.1419048.

[50] F. Guillou, H. Yibole, G. Porcari, L. Zhang, N.H. van Dijk, E. Brück, Magnetocaloric effect, cyclability and coefficient of refrigerant performance in the MnFe(P, Si, B) system, J. Appl. Phys. 116 (2014) 063903, https://doi.org/10.1063/1.4892406.

[51] F. Guillou, G. Porcari, H. Yibole, N. van Dijk, E. Brück, Taming the first-order transition in giant magnetocaloric materials, Adv. Mater. 26 (2014) 2671–2675, https://doi.org/10.1002/adma.201304788.

[52] K.P. Skokov, A.Yu Karpenkov, D.Yu Karpenkov, O. Gutfleisch, The maximal cooling power of magnetic and thermoelectric refrigerators with La(FeCoSi)13 alloys, J. Appl. Phys. 113 (2013) 17A945, https://doi.org/10.1063/1.4801424.

[53] O. Gutfleisch, A. Yan, K.-H. Müller, Large magnetocaloric effect in melt-spun LaFe13−xSix, J. Appl. Phys. 97 (2005) 10M305, https://doi.org/10.1063/1.1847871.

[54] T. Gottschall, K.P. Skokov, M. Fries, A. Taubel, I. Radulov, F. Scheibel, D. Benke, S. Riegg, O. Gutfleisch, Making a cool choice: the materials library of magnetic refrigeration, Adv. Energy Mater. 9 (2019) 1901322, https://doi.org/10.1002/aenm.201901322.

[55] E. Gaudin, S. Tencé, F. Weill, J. Rodriguez Fernandez, B. Chevalier, Structural and magnetocaloric properties of the new ternary silicides Gd6M5/3Si3 with M = Co and Ni, Chem. Mater. 20 (2008) 2972–2979, https://doi.org/10.1021/cm8000859.

[56] T.D. Thanh, D.C. Linh, P.D.H. Yen, L.V. Bau, V.H. Ky, Z. Wang, H.-G. Piao, N.M. An, S.-C. Yu, Magnetic and magnetocaloric properties in second-order phase transition La1−xKxMnO3 and their composites, Phys. B: Condens. Matter 532 (2018) 166–171, https://doi.org/10.1016/j.physb.2017.03.031.

[57] P.T. Long, T.V. Manh, T.A. Ho, V. Dongquoc, P. Zhang, S.C. Yu, Magnetocaloric effect in La1-xSrxCoO3 undergoing a second-order phase transition, Ceram. Int. 44 (2018) 15542–15549, https://doi.org/10.1016/j.ceramint.2018.05.216.